SUPPLEMENTAL MATERIAL

Origins of the unidirectional spin Hall magnetoresistance in metallic bilayers

Can Onur Avci,[1] Johannes Mendil,[2] Geoffrey S. D. Beach,[1] and Pietro Gambardella[2]

[1]*Department of Materials Science and Engineering, Massachusetts Institute of Technology, Cambridge, Massachusetts 02139, USA*

[2]*Department of Materials, ETH Zürich, CH-8093 Zürich, Switzerland*

CONTENTS

SM 1. Harmonic analysis of the nonlinear magnetoresistance

Figure S1 shows a schematic of the experimental setup and coordinate system employed in this work. We measured the longitudinal (R) and transverse resistance (R_H) by applying an ac current $I = I_0 \sin \omega t$ of frequency $\omega/2\pi =$ 10 Hz and recording the ac longitudinal (V) and transverse (V_H) voltages, respectively. The Ohm's law for a current-dependent resistance reads $V(I) = R(I) \cdot I_0 \sin(\omega t)$. Assuming that the nonlinear (current-induced) changes of $R(I)$ are small with respect to the linear resistance R_0, we expand $R(I)$ as follows:

$$R(I) = R_0 + \frac{dR}{dI} dI = R_0 + I_0 \frac{dR}{dI} \frac{dI}{dt} dt. \tag{S1}$$

Using $I(t) = I_0 \sin \omega t$ we obtain $R(I) = R_0 + I_0 \frac{dR}{dI} \cos \omega t \, \omega dt$, where $\omega = \frac{2\pi}{T}$ is the angular frequency, T the period, and $dt = \frac{T}{n}$ the time interval, with n being the number of measurements per period. The term $\omega dt = 2\pi/n$ is a constant and is normalized by the fast Fourier transform algorithm used in the experiment. Then, $V(I)$ becomes:

$$V(I) = I_0 R_0 \sin(\omega t) + \frac{1}{2} I_0^2 \frac{dR}{dI} \sin(2\omega t). \tag{S2}$$

The longitudinal voltage consists of first and second harmonic terms that scale with I_0 and I_0^2, respectively. Analogous expansions apply to the Hall voltage and Hall resistance. The first harmonic longitudinal resistance is $R_\omega = R_0$. The second harmonic longitudinal resistance $R_{2\omega} = \frac{1}{2} I_0 \frac{dR}{dI}$ consists of three contributions [1], namely the unidirectional magnetoresistance (UMR), the magnetothermal effects due to the temperature gradients (∇T) induced by Joule heating, and the spin-orbit torque (SOT) induced modulation of the total magnetoresistance:

$$R_{2\omega} = R_{2\omega}^{UMR} + R_{2\omega}^{\nabla T} + R_{2\omega}^{SOT}. \tag{S3}$$

Below we briefly explain the origin of each term.

Spin-orbit torques: This term occurs due to the current-induced oscillations of the magnetization that modulate the magnetoresistance through the dependence of the anisotropic magnetoresistance and spin Hall magnetoresistance on the polar (θ) and azimuthal (φ) angles of the magnetization ($\boldsymbol{m}$). Due to the symmetric behavior of the magnetoresistance with respect to the *xy* plane, the out-of-plane oscillations driven by the damping-like (DL) SOT

do not contribute to $R_{2\omega}$. The in-plane effective field ($b_{\varphi}^{SOT} \propto I$) associated to the field-like (FL) SOT and Oersted field, on the other hand, gives rise to a signal with the following symmetry:

$$R_{2\omega}^{SOT} = b_{\varphi}^{SOT}(I_0) \cdot (R^x - R^y) \frac{d \cos^2 \varphi}{dI}, \tag{S4}$$

where R^x and R^y are the resistance of the sample when the magnetization is parallel to the *x* and *y* axis, respectively. The dependence of the resistance in the *xy* plane follows a $\cos^2 \varphi$ function, therefore the current-induced oscillations in this plane are proportional to the derivative of this term with respect to the current[2].

Magnetothermal effects: This term occurs due to Joule heating and the corresponding quadratic increase of the sample temperature with current, which gives rise to temperature gradients

$$\nabla T \propto I_0^2 \sin^2(\omega t)\, R_0 = \frac{1}{2} I_0^2 [1 - \cos(2\omega t)] R_0. \tag{S5}$$

Depending on the direction of ∇T, the anomalous Nernst (ANE), spin Seebeck and magneto-thermopower effects can give rise to a longitudinal current-dependent electromotive force, which appears in the measurement of $R_{2\omega}$. In previous work[1,2], we demonstrated that in the geometry used for measuring the UMR only the out-of-plane temperature gradient ($\nabla \mathrm{T}_z$) and ANE give measureable contributions to $R_{2\omega}$, which have the form

$$R_{2\omega}^{\nabla T} \propto \nabla \mathrm{T}_z m_y. \tag{S6}$$

Unidirectional magnetoresistance: This term occurs due to the difference in resistance for opposite polarity of the injected current. As discussed in the main text, the UMR has three different contributions, namely the two SD-UMR terms originating from the bulk and interface spin-dependent scattering of the spin-polarized conduction electrons, and the SF-UMR originating from the spin-flip scattering induced by the electron-magnon interaction. The SD-UMR gives rise to a second harmonic resistance

$$R_{2\omega}^{\mathrm{SD}} \propto \theta_{SH}\, \boldsymbol{I} \times \boldsymbol{m} \propto I_0 \theta_{SH} m_y, \tag{S7}$$

where θ_{SH} is the spin Hall angle of the nonmagnetic metal layer (NM). The SF-UMR, on the other hand, is due to the modulation of the magnon density by the absorption of the SHE-induced spin current, which alters the electron-magnon scattering in the ferromagnetic layer and thereby the longitudinal resistance. Depending on the current

direction, magnons are effectively damped or amplified, which results in a current-dependent resistance term. Due to the strong dependence of the magnon density on temperature, we find that the spin-flip scattering terms scales as $T + \Delta T \propto const. + I^2$, where T is the sample temperature in the absence of Joule heating and $\Delta T \propto I^2$ is the temperature rise due to Joule heating. According to our measurements (see main text), the SF-UMR gives rise to a second harmonic resistance

$$R_{2\omega}^{\mathrm{SF}} \propto I_0 \theta_{SH}[T + \Delta T] \cdot B^{-p(T)} f(m_y) \propto \theta_{SH}[I_0 + I_0^3] \cdot B^{-p(I_0)} f(m_y), \tag{S8}$$

where B is the externally applied magnetic field, p is the exponent of the power law decay of electron-magnon scattering with applied field, and $f(m_y)$ is an odd function of m_y that can be expressed as a power series of $\frac{m_y}{m} + \left(\frac{m_y}{m}\right)^3 + \left(\frac{m_y}{m}\right)^5 + \cdots$. Combining equations S7 and S8 we obtain the general expression for the UMR

$$R_{2\omega}^{\mathrm{UMR}} = aI_0 + b(B)I_0 + c(B)I_0^3. \tag{S9}$$

where $a \propto I_0 \theta_{SH} m_y$, $b \propto \theta_{SH} B^{-p} f(m_y)$ and $c \propto \theta_{SH} B^{-p} f(m_y)$. Note that the UMR does not originate uniquely from the SHE but has contributions from all the different effects that contribute to charge-spin conversion in a ferromagnetic/normal metal bilayer, including the REE and related phenomena[3]. In this context, θ_{SH} is an effective parameter that accounts for the overall charge-spin conversion efficiency.

SM 2. Separation of the spin-orbit torque, magnetothermal, and magnetoresistive contributions to $R_{2\omega}$

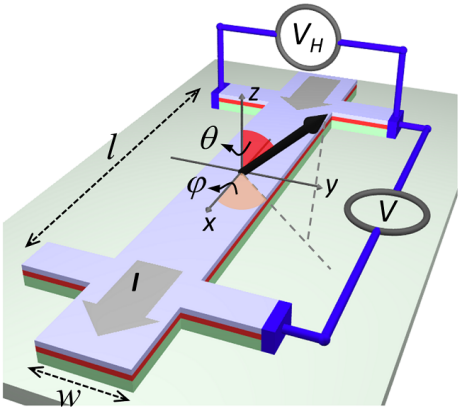

Figure S1. Schematic of the device structure and coordinate system.

In order to single out the UMR, both magnetothermal and SOT effects must be quantified. Since the SD-UMR and the magnetothermal voltages possess the same angular symmetry (see Eqs. S6 and S7), they cannot be quantitatively separated by measuring only the longitudinal $R_{2\omega}$. However, the SD-UMR does not manifest itself in the Hall effect measurements, whereas the magnetothermal voltages do. By employing this property, we can quantitatively extract the magnetothermal contribution from the longitudinal $R_{2\omega}$ following the method explained in detail in Ref. [1]. In brief, the procedure consists in performing angle-dependent measurements of the harmonic Hall resistances R_{ω}^{H} and $R_{2\omega}^{H}$ by rotating B in the *xy* plane and repeating the measurements for several amplitudes of B. As it is known from previous measurements[2], $R_{2\omega}^{H}$ depends on the polar (b_{θ}^{SOT}) and azimuthal (b_{φ}^{SOT}) components of the current-induced electric fields due to the SOT and Oersted field as well as on the ANE due to $\nabla \mathrm{T}_z$. The component b_{θ}^{SOT} is due to the damping-like (DL) SOT and is counteracted by the effective field $B_{eff} = B + B_a + B_d$, where B_a and B_d are the anisotropy field and demagnetizing field, respectively. The component b_{φ}^{SOT} is due to sum of the FL-SOT and Oersted field and is counteracted only by the external field (assuming no significant in-plane anisotropy, as is the case here). Thus, the effects of b_{θ}^{SOT} and b_{φ}^{SOT} on $R_{2\omega}^{H}$ are scaled by B_{eff} and B, respectively. Moreover, b_{θ}^{SOT} induces an out-of-plane tilt of the magnetization and therefore manifests itself through the anomalous Hall effect (AHE), whereas b_{φ}^{SOT} induces an in-plane tilt of the magnetization and therefore manifests itself through the planar Hall effect (PHE). The resulting expression for $R_{2\omega}^{H}$ is given by[2]

$$R_{2\omega}^{H} = \left(R_{AHE}\frac{b_{\theta}^{SOT}}{B_{eff}} + I_0\alpha\nabla \mathrm{T}_z\right)\cos\varphi + 2R_{PHE}\frac{b_{\varphi}^{SOT}}{B}(2\cos^3\varphi - \cos\varphi), \tag{S10}$$

where R_{AHE} and R_{PHE} are the anomalous and planar Hall resistances, respectively, and α is an effective coefficient that accounts for the ANE and the spin Seebeck effect. By isolating the term proportional to $\cos\varphi$ and analyzing its field dependence, one can unambiguously determine b_{θ}^{SOT} and the magnetothermal contribution $I_0\alpha\nabla \mathrm{T}_z$.

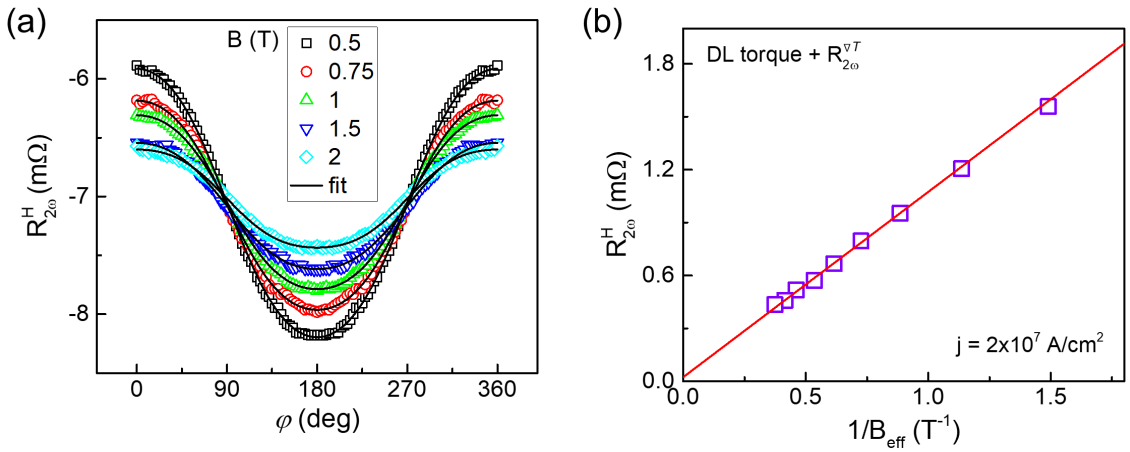

Figure S2. (a) Angular dependence of the second harmonic Hall resistance $R^H_{2\omega}$ of Co(2.5 nm)/Pt(6 nm) as the field B rotates in the xy plane. Black lines show the fits according to Eq. S10. (b) DL-SOT and magnetothermal contributions to $R^H_{2\omega}$ plotted as a function of 1/B$_{eff}$. The slope of the linear fit corresponds to the DL-SOT strength multiplied by R$_{AHE}$; the intercept corresponds to the field-independent magnetothermal contribution $R^{H,\nabla T}_{2\omega} = I_0 \alpha \nabla T_z$.

Figure S2(a) shows a series of measurements of $R^H_{2\omega}$ of Co(2.5 nm)/Pt(6 nm) taken at different fields with $j = 2 \times 10^7$ A/cm^2. We observe that the $\cos\varphi$ contribution to $R^H_{2\omega}$ dominates the signal, as expected because the DL-SOT is larger than the FL-SOT and $R_{AHE} \gg R_{PHE}$. By fitting $R^H_{2\omega}$ with Eq. S10, we obtain the coefficient $\left(R_{AHE}\frac{b_\theta^{SOT}}{B_{eff}} + I_0\alpha\nabla T_z\right)$. Figure S2(b) shows a plot of $\left(R_{AHE}\frac{b_\theta^{SOT}}{B_{eff}} + I_0\alpha\nabla T_z\right)$ as a function of $1/B_{eff}$. The linear scaling is in very good agreement with Eq. S10. We determine the magnetothermal contribution by taking the intercept of the linear fit with the y-axis, which indicates that $I_0\alpha\nabla T_z$ is about 0.02 mΩ. Finally, in order to convert the magnetothermal Hall resistance into a longitudinal resistance, we multiply $I_0\alpha\nabla T_z$ by the geometrical aspect ratio (length/width) of the Hall bar, which yields $R^{\nabla T}_{2\omega} = I_0\alpha\nabla T_z\frac{l}{w}$. Here, the factor $\frac{l}{w}$ is obtained by taking the ratio of the anisotropic magnetoresistance to the planar Hall resistance, which agrees with measurements of the sample dimensions performed by scanning electron microscopy.

By evaluating the slope and the intercept of such data, we characterized the DL-SOT and magnetothermal signals for all the samples reported in this study. Note that R_{AHE}, necessary to quantify the DL-SOT, is obtained by performing a Hall effect measurement using a large out-of-plane field (not shown).

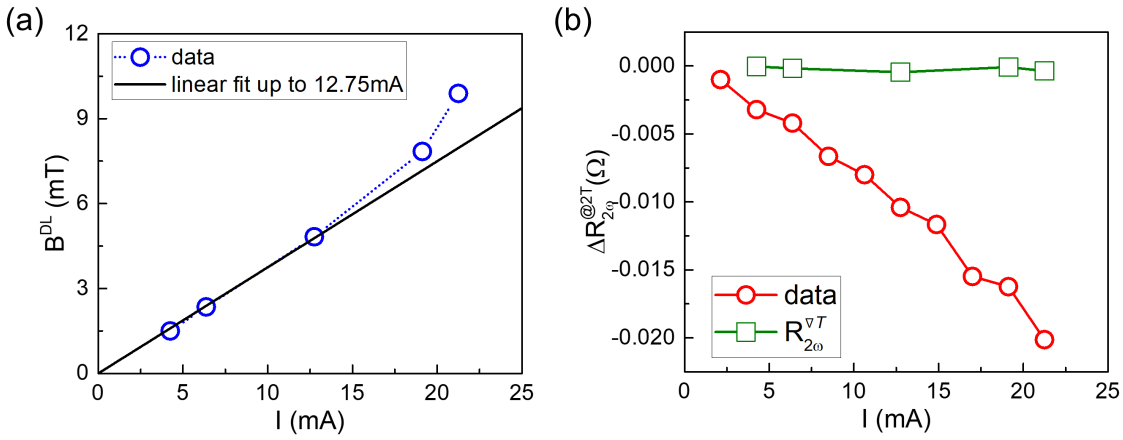

Figure S3. (a) Values of the DL-SOT derived from the linear fits shown in Fig.S2 (b). The values of the effective field are linearly proportional to the current up to 12.75 mA, which corresponds to j = 3x10^7 A/cm^2. The deviation from linearity at higher current may be due to Joule heating-induced changes of the anisotropy field and M_s. (b) Estimated thermal contribution to the longitudinal $R_{2\omega}$ signal recorded at $B = \pm 2$ T.

According to this analysis, the thermal contribution $R_{2\omega}^{\nabla T}$ to the longitudinal resistance is less than 4% of the total $R_{2\omega}$ signal in Co(2.5 nm)/Pt(6 nm) throughout the entire current range investigated in this work (Fig. S3). In the Pt(4 nm)/CoCr(t) series, on the other hand, the UMR is smaller and of the same order of magnitude as the magnetothermal signal. Detailed measurements of the SOT and $R_{2\omega}^{\nabla T}$ of CoCr(t)/Pt(4) are reported in Sect. SM 7.

SM 3. Estimation of the device temperature as a function of applied current

We estimate the current-induced Joule heating of our devices by comparing the change in the resistance as a function of current in ambient conditions to the change of resistance as a function of temperature. Figure S4 shows the result of such an analysis. We first record the temperature dependence of R near room temperature (268 – 298 K range). Then, we perform a linear fit and obtain the slope $\Delta R/\Delta T$ [Fig. S4(a)]. We then measure R in ambient conditions as a function of current [Fig. S4(b)]. We observe that R increases proportionally to I^2, as expected, since the heat generated by the injected current depends on the power applied on the device ($\Delta T \propto I^2 R$). Finally, we estimate the temperature rise with respect to room temperature as $\Delta T(I) = \left(\frac{\Delta R}{\Delta T}\right)^{-1} [R(I) - R(I \approx 0)]$, as shown in Fig. S4(c).

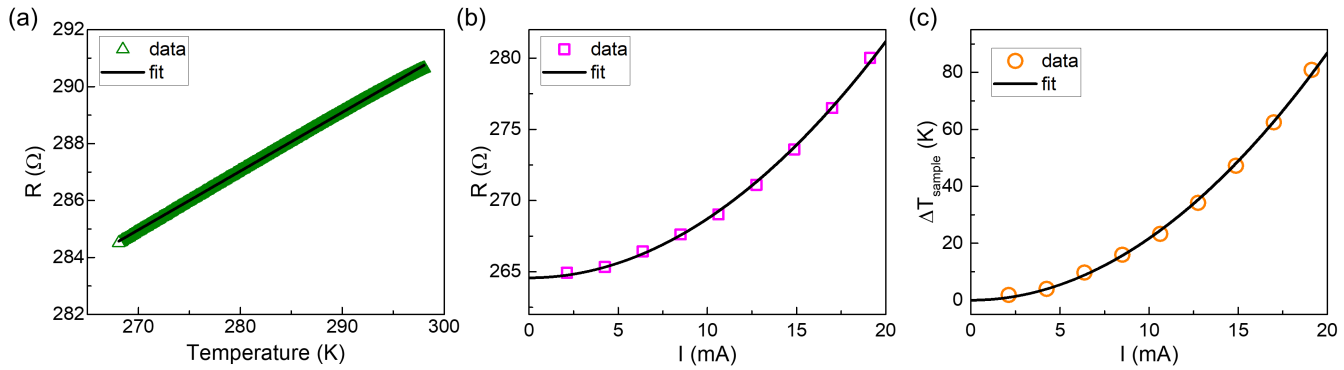

Figure S4. (a) Reference measurement of the resistance as a function of temperature. The solid line is a linear fit to the data. (b) Device resistance as a function of current, showing a quadratic increase (fit), as expected from Joule heating. (c) Device temperature as estimated from the relation between *R* and *T* found in (a).

SM 4. Spin disorder magnetoresistance due to electron-magnon scattering

The resistivity of a ferromagnet contains both nonmagnetic and magnetic terms. The nonmagnetic terms mainly arise from electron-phonon and electron-impurity scattering. The magnetic terms, as expected, depend strongly on the magnetic configuration and applied magnetic field. These terms include the anisotropic magnetoresistance, the domain wall magnetoresistance, and the spin disorder magnetoresistance. The latter, also called magnon magnetoresistance, arises from spin flip scattering due to the interaction of the conduction electrons with thermally excited magnons[4,5]. A signature of this effect in thin films is an almost linear and nonsaturating negative magnetoresistance in the single-domain magnetic state, due to the damping of magnons at high fields[6,7].

Figure S5 (a) shows the first harmonic measurements of R_ω as a function of field applied parallel to y. These measurements exhibit the typical magnetoresistive behavior of ferromagnetic thin films, with a sharp peak due to domain reorientation near $B = 0$ and a linear negative magnetoresistance at high field due to the decrease of spin disorder in the saturated state. Of interest to the present study is the fact that the slope of negative magnetoresistance at high field, $\left.\frac{\partial R_\omega}{\partial B}\right|_{B \geq 1\ \mathrm{T}}$, changes proportionally to I^2 [Fig. S5 (b)], indicating that Joule heating significantly increments the magnon population as the temperature changes by an amount $\Delta T \propto I^2$. Therefore, in agreement with

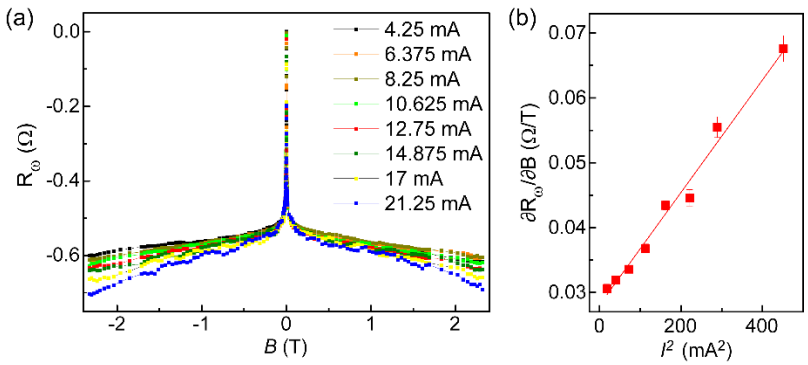

Figure S5. (a) Magnetoresistance of Co(2.5)/Pt(6) as a function of $B \parallel y$. The curves show $R_\omega(B,\ I) - R_\omega(0,\ I)$ for different current levels. The current ranges from 4.25 mA ($j = 1 \times 10^7$ A/cm^2) to 21.25 mA ($j = 5 \times 10^7$ A/cm^2). (b) $\frac{\partial R_\omega}{\partial B}$ evaluated for $B \geq 1\,T$ as a function of I^2. The line is a linear fit to the data.

the Rayleigh-Jeans approximation of the Bose-Einstein distribution function, we expect that the magnon density in our samples will be proportional to $T + \Delta T \propto const. + I^2$, where T is the ambient temperature (the sample's temperature in the absence of current).

SM 5. Fits of the current, field and magnetization angle dependence of $R_{2\omega}$

We first analyze the current dependence of $R_{2\omega}$ reported in the main text [Fig. 2(d)], also shown below in Fig. S6(a). For $\varphi = 90°$, we find that the function

$$\frac{\Delta R_{2\omega}^{\mathrm{UMR}}}{R} = [a + b(B)]I_0 + c(B)I_0^3 \tag{S11}$$

fits the data accurately at different currents and fields [solid lines in Fig. S6(a)]. Figure S6(b) and (c) show the fit results for $[a + b(B)]$ and $c(B)$ as a function of B. We see that these coefficients are larger at low field and rapidly decay as B increases. We attribute this strong field dependence to the damping of ambient temperature (coefficient b) and current-induced (coefficient c) magnons by the external field.

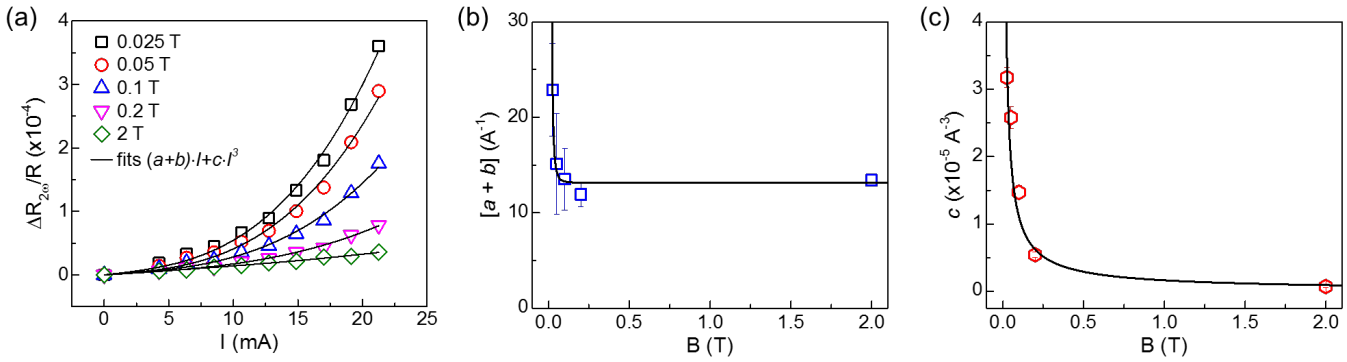

Figure S6. (a) Fits of the current dependence of the UMR in Pt(6 nm)/Co(2.5 nm) according to Eq. S11. (b,c) Field dependence of the fit coefficients $[a + b(B)]$ and $c(B)$. The solid lines are fits to B^{-p}.

We now turn to the field-dependent decay of the UMR signals at constant current. In order to obtain quantitative insight into the dependence of the UMR on the field-induced magnon damping, we fit the SF-UMR given by $|R_{2\omega}(B) - R_{2\omega}(B = 2\ T)|$ with the following empirical expression:

$$|R_{2\omega}(B) - R_{2\omega}(B = 2\ T)| = \frac{r}{B^p}\,. \qquad \text{(S12)}$$

Here r is the signal amplitude that scales with the injected current and p is an exponent that is expected to be close to 1 based on models of the negative magnetoresistance due to electron-magnon scattering[6,8]. Notice that the subtraction of the signal measured at 2 T effectively eliminates the SD-UMR from the total signal. Figure 2(b) in the main text shows the results of the fits using Eq. S12 for different current densities in Co(2.5 nm)/Pt(6 nm). In order to avoid the low field region where the magnetization is nonuniform, we restricted the fits to $B \geq 50$ mT.

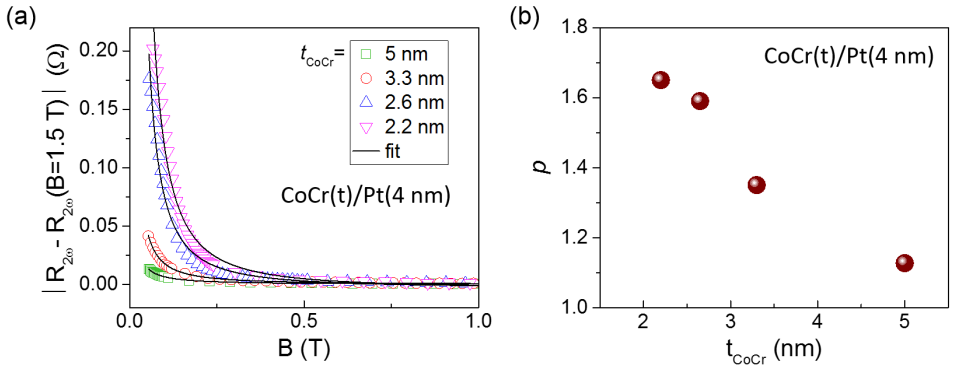

Figure S7. (a) Fits of the field dependence of the SF-UMR of CoCr(t)/Pt(4 nm). (b) Values of the exponent p plotted as a function of the CoCr thickness. The current density for all CoCr samples was kept at $j \sim 2.5\text{x}10^7$ A/cm^2.

We find excellent agreement between the data and Eq. S12 by letting the exponent p vary depending on the current density. We find that p increases monotonically from 0.61 to 0.86 as j varies from 1 to 5x10^7 A/cm^2, as expected due to the temperature-induced renormalization of the magnon mass in thin Co films[8]. In other words, as the temperature increases the magnon dispersion "softens" and the magnon density of states increases, leading to a stronger dependence of the SF-UMR on the applied magnetic field. Another effect related to the magnon stiffness appears in the field dependence of the SF-UMR of the CoCr/Pt series, where we observe that p decreases from about 1.7 to 1.1 as a function of CoCr thickness (Fig. S7). We attribute such a decrease to the strong increase of the magnon stiffness that occurs in thin films during the cross-over from two-dimensional to three-dimensional behavior[7]. Accordingly, a stronger field is required to suppress the current-induced creation and annihilation of magnons in thicker films relative to thin films.

Finally, we discuss the fitting of angular dependence of $R_{2\omega}$ appearing in Fig. 3 of the main text. The contribution of the SD-UMR and spin-orbit torques to $R_{2\omega}$ are proportional to $\sin\varphi$ and $\sin\varphi\cos^2\varphi$, respectively. The angular dependence of the SOT signal can be understood by examining Eq. S4 and the effective fields acting on **m** corresponding to the FL, Oersted and DL torques. For in-plane magnetization the DL-SOT generates out-of-plane oscillations to **m** whose signal is proportional to $\left(\frac{d\sin^2\theta}{d\theta}\Big|_{\theta=90^\circ}\right)$ which is zero due to symmetric variation of the magnetoresistance for up and down tilting of **m** around $\theta = 90°$, where θ is the polar angle of the magnetization with respect to the z-axis. However the Oersted and FL effective fields contribute to $R_{2\omega}^{SOT}$ as noted in Eq. S4. This signal is proportional to $(d\cos^2\varphi/dI)$ where the derivative can be replaced by $d\varphi$ without losing generality, thereby yielding $R_{2\omega}^{SOT} \propto (\sin\varphi\cos\varphi)$. Finally By taking into account the geometrical factor of the effective field $\mathbf{b}^{FL,Oe} \propto \mathbf{m}\times\mathbf{T}^{FL,Oe} \propto \cos\varphi$ we obtain the final angular form of the SOT term as $R_{2\omega}^{SOT} \propto (\sin\varphi\cos^2\varphi)$.

In order to capture the peaked angular dependence of the SF-UMR around $\varphi = 90°$ and $270°$, we have to consider higher order terms in $\sin\varphi$ in the cumulative expression of the second harmonic resistance. We therefore assume that $R_{2\omega}(\varphi)$ is given by

$$R_{2\omega}(\varphi) = R_{2\omega}^{SD} \sin\varphi + R_{2\omega}^{SF1} \sin\varphi + R_{2\omega}^{SF3} \sin^3\varphi + R_{2\omega}^{SF5} \sin^5\varphi + R_{2\omega}^{SOT} \sin\varphi \cos^2\varphi, \qquad \text{(S13)}$$

where $R_{2\omega}^{SD}$ and $R_{2\omega}^{SOT}$ represent the amplitude of the SD-UMR and spin-orbit torque contribution to $R_{2\omega}$, and $R_{2\omega}^{SF1,3,5}$ are the expansion coefficients of the angular dependence of the SF-UMR. Because of the presence of different odd terms in $\sin\varphi$, a fit of $R_{2\omega}(\varphi)$ using Eq. S13 is overparametrized. Therefore, to extract plausible values of the fit coefficients, we have first fitted the high-field curve (B = 2 T) with a simple sine function to find the SD-UMR contribution, assuming that the $R_{2\omega}^{SOT}$ and $R_{2\omega}^{SF}$ are negligible in this measurement. We then fitted the low-field data by setting $R_{2\omega}^{SD}$ equal to that obtained at high-field. We have realized that the choice of $R_{2\omega}^{SOT}$ strongly affects the parameter set for the different $R_{2\omega}^{SF}$ coefficients. To tackle this issue, we have estimated $R_{2\omega}^{SOT}$ by analyzing the transverse Hall signal $R_{2\omega}^{H}$ recorded simultaneously with $R_{2\omega}$. We then fixed $R_{2\omega}^{SOT}$ to that estimated and left the $R_{2\omega}^{SF1,3,5}$ terms as free parameters. For the low-current data, the higher order terms, namely $R_{2\omega}^{SF3}$ and $R_{2\omega}^{SF5}$, are negligibly small. On the other hand, for the high-current data, nonzero $R_{2\omega}^{SF3}$ and $R_{2\omega}^{SF5}$ are required to fit the data. A similar result, albeit with a much reduced $R_{2\omega}^{SF3}$ term compared to $R_{2\omega}^{SF5}$, is obtained by letting $R_{2\omega}^{SOT}$ vary as free parameter. The fit parameters obtained by using the two approaches are reported in Table S1. Despite the uncertainty in the relative weight of $R_{2\omega}^{SF3}$ and $R_{2\omega}^{SF5}$ for the high-current data, these results indicate that the higher order terms are essential to fit the observed peaked behavior around $\varphi = 90°$ and 270° and that the interaction between magnons and the injected spin current becomes highly efficient when the magnetization is collinear with the spin polarization direction, leading to a nonlinear angular and current dependence.

Table S1 – Fit parameters obtained for the low-field data reported in Fig.3 (b) and (d) of the main text. All parameters are in units of mΩ. The gray boxes indicate fixed parameters used for the fits. Left sub-column of $R_{2\omega}^{SOT,SF1,3,5}$ correspond to the fitting results obtained by fixing $R_{2\omega}^{SOT}$ to the estimated value determined by the harmonic Hall measurements. Right sub-columns correspond to fitting by leaving all four parameters free, i.e. $R_{2\omega}^{SOT}$ and $R_{2\omega}^{SF1,3,5}$.

	$R_{2\omega}^{SD}$	$R_{2\omega}^{SOT}$		$R_{2\omega}^{SF1}$		$R_{2\omega}^{SF3}$		$R_{2\omega}^{SF5}$	
Co(2.5)/Pt(6) – 4.25 mA	-1.1	-1.0	-0.94	-3.23	-3.4	0	0	0	0
Co(2.5)/Pt(6) – 21.25 mA	-8.8	-5.5	-10.9	-54.7	-11	73.5	19.9	-77.3	-77.3

SM 6. Temperature dependence of the UMR in Co/Pt bilayers

By analyzing the current dependence of the UMR signals we have revealed that the SF-UMR is a strongly temperature-dependent process whereas the SD-UMR is not. Temperature dependent measurements in the range of 4 – 300 K confirm this hypothesis and provide further evidence that the SF and SD-UMR originate from different resistive mechanisms.

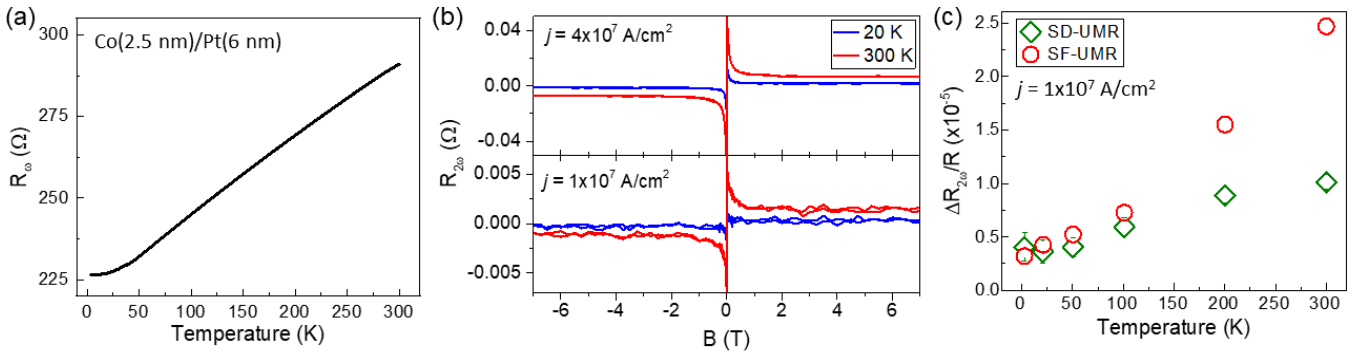

Figure S8. (a) Temperature dependence of the longitudinal resistance of Co(2.5 nm)/Pt(6 nm) measured with j = 1x10^7 A/cm^2. (b) $R_{2\omega}(B, I)$ as a function of B recorded at 20 K and 300 K for large (j = 4x10^7) and moderate (j = 1x10^7) current density (a constant offset is removed from the curves for ease of comparison). (c) SF-UMR and SD-UMR as a function of the nominal sample temperature.

Although the UMR is much more prominent at high current density, in order to avoid excessive heating at low temperature, we have limited the current density to $j = 1 \times 10^7$ A/cm^2. Figure S8 (a) shows the temperature dependence of the longitudinal resistance. Expectedly, the resistance decreases as the temperature is lowered in a quasi-linear fashion down to 50 K. For comparison, we measured the device resistance for $j = 4 \times 10^7$ A/cm^2 at a set temperature of 4 K (not shown). The sample temperature is estimated to be ~75 K, thus showing a strong Joule heating effect for relatively large j at low temperature (note that Joule heating has a stronger effect on temperatures below 100 K than it has at 300 K due to the reduced heat capacity of metals at low temperature). Figure S8(b) shows $R_{2\omega}$ measured as a function of $B \parallel \boldsymbol{y}$ at T = 300 K and 20 K. We observe that the low field enhancement of the signal associated to the SF-UMR is more prominent at 300 K than at 20 K, in agreement with the larger population of magnons at high temperature. Figure S8(c) summarizes the results obtained for the SF- and SD-UMR as a function of temperature. We find a ten-fold decrease of the SF-UMR between 300 K and 4 K, whereas the SD-

UMR decreases by a about factor of two in the same temperature range. This strong (weak) temperature dependence of the SF (SD) contributions to the UMR is consistent with the different origin of the two effects. For completeness, we remark that, even at a current density of $j = 1 \times 10^7$ A/cm^2, there may be deviations from the real and nominal temperature plotted in Fig. S8 (c), especially below 100 K.

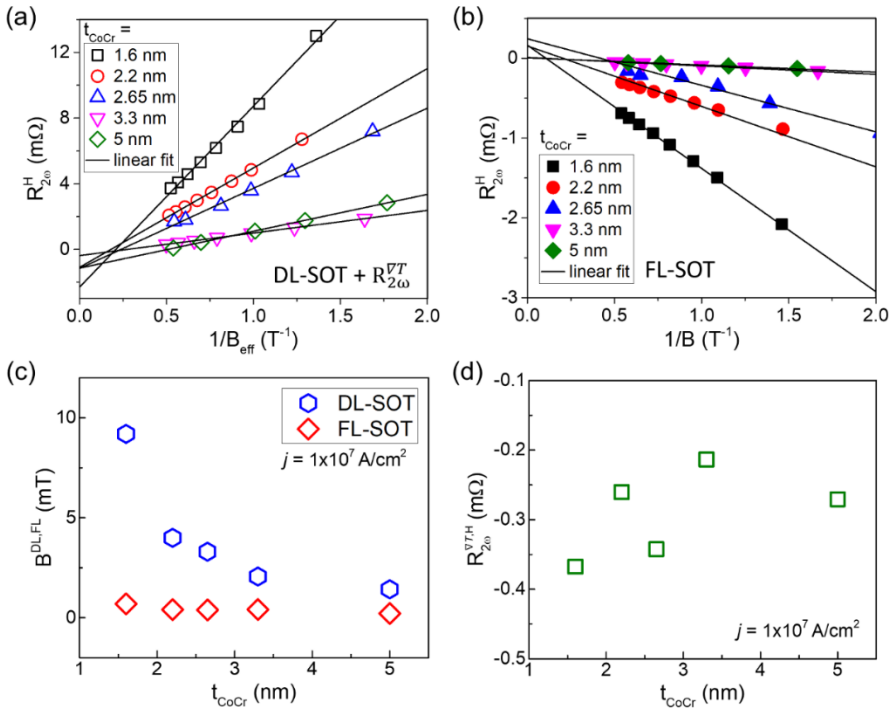

Figure S9. Spin-orbit torque and magnetothermal characterization of $Co_{80}Cr_{20}$(t)/Pt(4 nm). All measurements are performed at room temperature. (a) Plot of $R_{AHE}\frac{b_\theta^{SOT}}{B_{eff}} + I_0\alpha\nabla T_z$ as a function of $1/B_{eff}$. (b) Plot of $2R_{PHE}\frac{b_\varphi^{SOT}}{B}$ as a function of $1/B$. See Eq. S10 for more details. (c) Current-induced effective fields due to the DL-SOT and FL-SOT (including the Oersted field) normalized to $j = 1 \times 10^7$ A/cm^2. (d) Magnetothermal contribution to the second harmonic transverse resistance.

SM 7. Spin-orbit torques, anomalous Nernst effect, magnetoresistance, and UMR of $Co_{80}Cr_{20}$(t)/Pt(4 nm).

In this section we present a comprehensive characterization of the SOTs, magnetothermal effects, and UMR in the $Co_{80}Cr_{20}$(t)/Pt(4 nm) series by means of second harmonic Hall effect measurements. We follow the method briefly described in Sects. SM 1 and SM 2 (see Refs.[1,2,9] for more details) to identify the Hall signals with DL-SOT and magnetothermal origin [$\propto cos\varphi$, see Fig. S9 (a)], and FL-SOT origin [$\propto (2\cos^3\varphi - \cos\varphi)$, see Fig. S9 (b)]. Figure S9 (c) and (d) show the dependence of the SOT and magnetothermal effect (predominantly driven by the

ANE), respectively, as a function of $Co_{80}Cr_{20}$ thickness. We observe that the absolute magnitude of both the FL and DL torque decreases as the $Co_{80}Cr_{20}$ thickness increases. This result is expected, since the effect of the torques on the magnetization scales inversely with the magnetic volume of the sample. We also notice that the DL-SOT is significantly larger than the FL-SOT. This result is also in agreement with previous measurements of the DL- and FL-SOT in relatively thick ferromagnetic films ($\gtrsim$ 2 nm) [2,8], and is ascribed to the fact that the spin accumulation in the ferromagnetic layer rotates away from $\boldsymbol{y}$ as it diffuses into the ferromagnet, which leads to a fast decrease of the FL torque.

Finally, in Fig. S10 we show representative measurements of the first and second harmonic longitudinal signals $R_\omega(\varphi)$ and $R_{2\omega}(\varphi)$, respectively, that are used to evaluate the UMR of $Co_{80}Cr_{20}$/Pt reported in Fig.4 of the main text. Figures S10(a) and (b) show that the $R_\omega(\varphi)$ of "thin" (1.6 nm) and "thick" (3.3 nm) $Co_{80}Cr_{20}$/Pt is proportional to $\cos^2\varphi$, as expected for the anisotropic magnetoresistance and spin Hall magnetoresistance of a typical ferromagnet/nonmagnet bilayer. Figures S10(c) and (d) show the $R_{2\omega}(\varphi)$ measured simultaneously with $R_\omega(\varphi)$. The angular dependence of $R_{2\omega}(\varphi)$ follows Eq. S3. The green solid line is the magnetothermal signal $R_{2\omega}^{\nabla T}$ estimated with the procedure outlined in Sect. 2. The remaining contributions, due to $R_{2\omega}^{SOT}$ and $R_{2\omega}^{UMR}$, are shown by dashed and dotted lines, respectively. These data are measured at B = 1.85-1.9 T, such that the SF-UMR is negligible at this field.

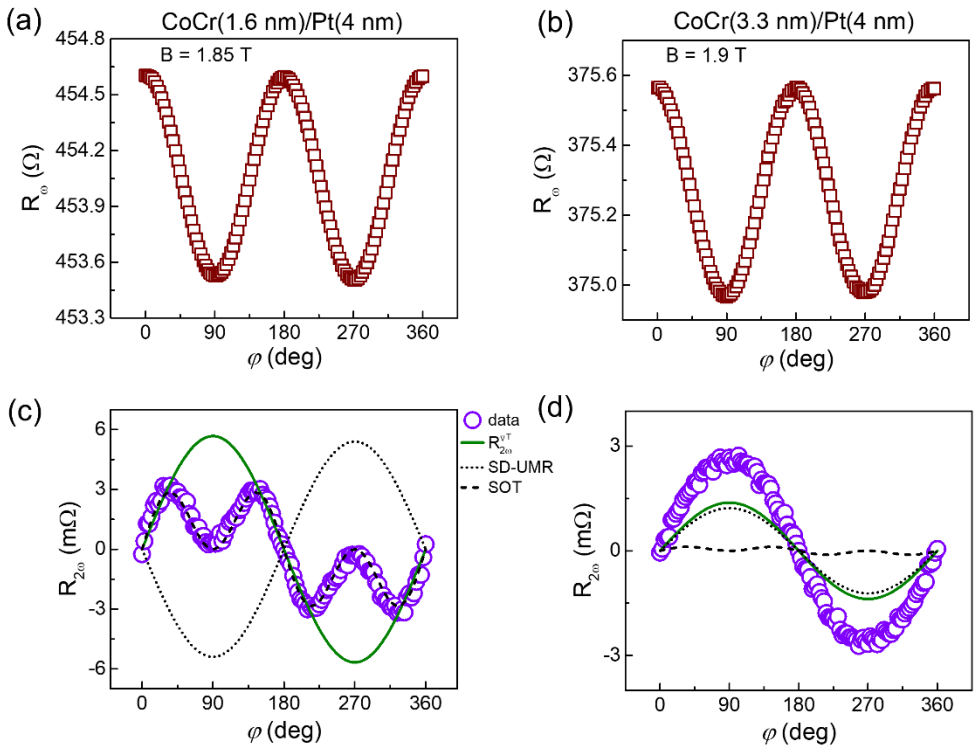

Figure S10. (a,b) $R_\omega(\varphi)$ and (c,d) $R_{2\omega}(\varphi)$ for two different thicknesses of $Co_{80}Cr_{20}$(t)/Pt(4 nm) measured at room temperature with B = 1.9 T. The solid green lines are the estimated ANE contributions whereas the dotted and dashed lines show SD-UMR and FL-SOT contributions, respectively. Note that, due to the reduced thickness of $Co_{80}Cr_{20}$(1.6 nm), the FL-SOT contribution to $R_{2\omega}(\varphi)$ is sufficiently large so as to produce a comparable signal to the SD-UMR.

References

[1] C. O. Avci, K. Garello, A. Ghosh, M. Gabureac, S. F. Alvarado and P. Gambardella, *Unidirectional spin Hall magnetoresistance in ferromagnet/normal metal bilayers*, Nat. Phys. **11,** 570 (2015).

[2] C. O. Avci, K. Garello, M. Gabureac, A. Ghosh, A. Fuhrer, S. F. Alvarado and P. Gambardella, *Interplay of spin-orbit torque and thermoelectric effects in ferromagnet/normal-metal bilayers*, Phys. Rev. B **90,** 224427 (2014).

[3] V. P. Amin and M. D. Stiles, *Spin transport at interfaces with spin-orbit coupling: Phenomenology*, Phys. Rev. B **94,** 104420 (2016).

[4] T. Kasuya, *Electrical Resistance of Ferromagnetic Metals*, Progr. Theor. Phys **16,** 58 (1956).

[5] D. A. Goodings, *Electrical Resistivity of Ferromagnetic Metals at Low Temperatures*, Phys. Rev. **132,** 542 (1963).

[6] A. P. Mihai, J. P. Attané, A. Marty, P. Warin and Y. Samson, *Electron-magnon diffusion and magnetization reversal detection in FePt thin films*, Phys. Rev. B **77,** 60401 (2008).

[7] R. M. Rowan-Robinson, A. T. Hindmarch and D. Atkinson, *Enhanced electron-magnon scattering in ferromagnetic thin films and the breakdown of the Mott two-current model*, Phys. Rev. B **90,** 104401 (2014).

[8] B. Raquet, M. Viret, E. Sondergard, O. Cespedes and R. Mamy, *Electron-magnon scattering and magnetic resistivity in 3 d ferromagnets*, Phys. Rev. B **66,** 24433 (2002).

[9] C. O. Avci, K. Garello, J. Mendil, A. Ghosh, N. Blasakis, M. Gabureac, M. Trassin, M. Fiebig and P. Gambardella, *Magnetoresistance of heavy and light metal/ferromagnet bilayers*, Appl. Phys. Lett. **107,** 1 (2015).

[10] T. D. Skinner, M. Wang, A. T. Hindmarch, A. W. Rushforth, A. C. Irvine, D. Heiss, H. Kurebayashi and A. J. Ferguson, *Spin-orbit torque opposing the Oersted torque in ultrathin Co/Pt bilayers*, Appl. Phys. Lett. **104,** 62401 (2014).